Remote Sensing of Environment 169 (2015) 232–242

Contents lists available at ScienceDirect

Remote Sensing of Environment

journal homepage: www.elsevier.com/locate/rse

Standing water effect on soil moisture retrieval from L-band passive microwave observations

N. Ye [a], J.P. Walker [a,*], J. Guerschman [b], D. Ryu [c], R.J. Gurney [d]

[a] Department of Civil Engineering, Monash University, Australia
[b] Land and Water Division, CSIRO, Australia
[c] Department of Infrastructure Engineering, University of Melbourne, Australia
[d] Environmental Systems Science Centre & National Centre for Earth Observation, University of Reading, United Kingdom

ARTICLE INFO

Article history:
Received 7 November 2013
Received in revised form 19 June 2015
Accepted 13 August 2015
Available online xxxx

Keywords:
Passive microwave remote sensing
Soil moisture
Water fraction

ABSTRACT

Passive microwave remote sensing at L-band has been widely acknowledged as the most promising technique to observe the spatial distribution of near surface (top ~5 cm) soil moisture at regional to global scales. The launch of the ESA's Soil Moisture and Ocean Salinity (SMOS) mission in 2009 now means that global space-borne brightness temperature observations are available at L-band (1.41 GHz) to estimate soil moisture every 2 to 3 days with a target accuracy of 0.04 m^3/m^3. Moreover, NASA's Soil Moisture Active Passive (SMAP) satellite has been launched on 31st January 2015, also carrying an L-band radiometer, together with an L-band radar for downscaling the brightness temperature observations to better than 10 km resolution. At the SMOS/SMAP radiometer scale of ~40 km, the presence of water bodies potentially induces an overestimation of retrieved soil moisture, if not carefully accounted for in retrieval models. Such water fraction effects on brightness temperature and soil moisture retrieval accuracy were investigated in this study, using airborne L-band brightness temperature data collected during three Australian field experiments. The water induced brightness temperature effect and water fraction were compared under different resolutions, sampling days, and land surface conditions, showing that the water fraction impact on retrieved soil moisture is independent of scale, but heavily dependent on the soil water content status. Subsequently, the highest water fraction threshold that can be tolerated in order to achieve the 0.04 m^3/m^3 target accuracy without correction has been determined as 0.08 (actual range is from 0.02 for dry bare soil to 0.08 for wet vegetated soil). Using a MODIS derived water fraction dataset, the water fraction dynamics were also studied over Australia during the ten years from 2001 to 2010. The results show that if the mean water fraction map was used as a static water map to flag or correct water effects, the water body induced soil moisture retrieval error would have exceeded the 0.04 m^3/m^3 target more than once for 13.5% of the Australian land 40 km sized radiometer pixels; only 0.6% Australian land pixels would have exceeded this target with a frequency of 10 times or more per year.

1. Introduction

Soil moisture is a key variable in global water, energy, and carbon cycles as it affects the partitioning of rainfall into runoff, vegetation evapotranspiration and microorganism activity (Aubert, Loumagne, & Oudin, 2003; Olioso, Chauki, Courault, & Wigneron, 1999; Schnürer, Clarholm, Boström, & Rosswall, 1986). The measurements of soil moisture in both time and space are required for many research disciplines such as hydrology, meteorology, and agriculture (Sellers et al., 1997). Due to its high temporal and spatial variability, soil moisture is difficult to be measured at regional to global scales (Crow et al., 2012; Ryu & Famiglietti, 2006).

Over the last 30 years remote sensing techniques have been developed to estimate the spatial distribution of surface soil moisture using electromagnetic radiation emitted or reflected from the earth in the range of visible, infrared and microwave frequencies. Among these approaches, the passive microwave technique at L-band (1–2 GHz) has been widely acknowledged as the most promising for water content measurement in the top ~5-cm soil layer, since it is independent of solar illumination, is capable to penetrate cloud, is least sensitive to vegetation canopy and surface roughness, and is directly related to volumetric water content through the soil dielectric constant. Hence, the first space mission dedicated to soil moisture is based on this approach; the European Space Agency (ESA) led Soil Moisture and Ocean Salinity (SMOS) satellite which employs a 2-D interferometric radiometer operating at L-band (1.41 GHz) to provide global soil moisture every 2–3 days (Kerr et al., 2010b). Moreover, the National Aeronautics and Space Administration (NASA) launched the Soil Moisture Active Passive

* Corresponding author.
E-mail address: jeff.walker@monash.edu (J.P. Walker).

http://dx.doi.org/10.1016/j.rse.2015.08.013
0034-4257/

(SMAP) mission on 31st January 2015, also with an L-band (1.41 GHz) radiometer. The SMAP will also have an L-band (1.2 GHz) radar for downscaling the radiometer brightness temperature observations (Entekhabi et al., 2010). Both missions aim to provide near surface soil moisture measurements with a target accuracy of 0.04 m^3/m^3, but the soil moisture retrieval may suffer from land surface heterogeneity within the sensor's ~40-km field-of-view, if it is not accounted for in the retrieval algorithm (Merlin et al., 2008).

The brightness temperature of soil is dependent mainly on the physical temperature of the soil layer and its emissivity, which is in turn determined by the soil dielectric constant and surface roughness. Due to the large difference between the (real part) dielectric constants of soil particles (~2) and water (~80), the microwave brightness temperature observation is highly sensitive to the water content of soil. Due to the relationship between soil water content and brightness temperature, soil moisture can be retrieved from brightness temperature observations. However, the presence of water bodies within the sensor's field-of-view will result in an overestimation in retrieved soil moisture. The effect of water fraction has been addressed in the SMOS Algorithm Theoretical Basis Document, by stating that approximately 1% underestimation of standing water fraction in the field-of-view can induce 0.01 m^3/m^3 soil moisture retrieval error under the conditions of wet (water content of 0.4 m^3/m^3) soil and dense (optical depth of 0.6) vegetation (Kerr et al., 2010a). Consequently, the SMAP mission proposes to use the on-board radar to map dynamic water bodies, but the ability to do this will be limited by the 3-km spatial resolution of the radar (Kim et al., 2012). Thus it is important to have a good understanding of the water body fraction that can be tolerated, particularly the cumulative effect from flood irrigation and small farm dams.

Model simulation (Davenport, Sandells, & Gurney, 2008; Loew, 2008) and a study using space-borne data and in-situ measurements (Gouweleeuw, van Dijk, Guerschman, Dyce, & Owe, 2012) have been conducted to investigate the effect of water fraction on brightness temperature and soil moisture retrieval accuracy. While these results show that the presence of standing water over less than 0.05 of a pixel could introduce an error in retrieved soil moisture as high as 0.2 m^3/m^3, the effect of water fraction on brightness temperature has not been verified using experimental data. Consequently, the objective of this study is to use airborne L-band passive microwave observations and in-situ ground measurements collected over SMOS/SMAP pixel sized areas to i) investigate the relationship between water fraction and impact on both the brightness temperature and the retrieved soil moisture, when ignoring the presence of water bodies in the soil moisture retrieval models, and ii) determine the extent of SMOS/SMAP pixels in Australia that could be adversely affected as a consequence.

2. Data sets and study areas

This study uses airborne passive microwave observations at L-band together with coincident ground sampling data collected during three field experiments. The National Airborne Field Experiment in 2006 (NAFE'06; Merlin et al., 2008) and Australian Airborne Cal/val Experiments for SMOS (AACES-1 and −2; Peischl et al., 2012) were conducted in the Murrumbidgee River Catchment, southeast of Australia. The ~82,000 km^2 Murrumbidgee River Catchment has an elevation ranging from ~40 m in the western plains to ~2000 m in the eastern mountainous areas. The annual rainfall varies from 300 mm in the west to 1900 mm in the high elevated ranges in the east (Australian Bureau of Rural Science, 2001). Accordingly, the land surface of the Murrumbidgee River Catchment varies from bare soil with sparse vegetation in the west, to irrigated fields mixed with grasslands in the middle, and to forest in the east. The location of the study areas, monitoring stations, flight lines, and calibration lakes of all three experiments are shown in Fig. 1.

2.1. Airborne instruments and pre-processing

The main airborne instrument used during the campaigns is the Polarimetric L-band Multi-beam Radiometer (PLMR) which was mounted on a scientific aircraft measuring L-band brightness temperature of the ground. The PLMR is a dual-polarized (vertically and horizontally) six-beam radiometer operating at 1.401–1.425 GHz. In push-broom configuration, the six beams of the PLMR are aligned in the across-track direction with view angles of 7°, 21.5°, and 38.5° to both sides of the aircraft, while in multi-angle configuration the PLMR is rotated by 90° such that all six beams are oriented along the flight direction. Each observation has a 3-dB beamwidth of 17° along-track and 14° across-track. During each sampling day, an approximately 6-hour flight was performed to map brightness temperature over a SMOS/SMAP sized area with a resolution of 1 km, or over a smaller area with a higher resolution.

Before and after each flight the PLMR was calibrated using the sky as a cold target and an instrumented blackbody as a hot target. After applying pre- and post-flight calibration the PLMR has an overall accuracy of better than 2 K (Panciera et al., 2008). In addition, a large water body around the study areas, e.g. Tombullen water storage for NAFE'06 and Lake Wyangan for AACES (see Fig. 1), was used as an inflight calibration check of the PLMR for each flight. In this study, the brightness temperature observations over the calibration lakes were also used to determine the range of brightness temperature of water bodies during the experimental periods.

To make brightness temperature observations comparable between different resolutions, sampling days, and land surface conditions, the original brightness temperature observations collected at multiple viewing angles were normalized to a reference angle of 38.5° using the approach outlined in Ye, Walker, and Rüdiger (2015), and the temporal variation of land surface temperature during the flight was corrected to a standard time using a ratio-based method (Jackson, 2001). During the ~6-hour flight in each sampling day, the surface soil moisture did not change by more than 0.005 m^3/m^3 unless it was actually raining, while the soil and vegetation temperature variations were up to 8 K. This temperature induced temporal variation of the PLMR brightness temperature observations was corrected by multiplying each brightness temperature observation with the ratio of effective soil temperature at the time of observation to that at an approximately mid-flight reference time, being 12:00 pm for the NAFE'06 and 6:00 am for the AACES.

The effective soil temperature at each time step was calculated from the time series of surface soil moisture, surface soil temperature, and deep soil temperature collected from the monitoring stations within the study area, using the method of Choudhury, Schmugge, and Mo (1982). With the temporal correction, the bias of the brightness temperature observations between repeat flights at the start and end of the data collection period reduced to less than 1 K, which is insignificant in comparison with the brightness temperature uncertainty that could be induced by standing water. The temporally corrected brightness temperature observations were then normalized to the viewing angle of the PLMR outer beams (38.5°, which is approximately the SMAP viewing angle) as the reference incidence angle for the purpose of providing complete coverage at a single incidence angle.

2.2. Monitoring station network

Since 2001 the OzNet hydrological monitoring network (www.oznet.org.au; Smith et al., 2012) has been operating throughout the Murrumbidgee River Catchment. It currently has 62 stations for continuous measurement of near surface soil moisture at 0–5 cm/0–8 cm, with many also having soil moisture measurements for 0–30 cm, 30–60 cm, and 60–90 cm. Soil moisture is measured using the Steven's Water Hydraprobe and CS616 water reflectometers. The soil temperature is measured at 2.5 cm and 15 cm, and rainfall using a tipping bucket rain gauge. Fig. 2 shows the time series of the spatially averaged near-

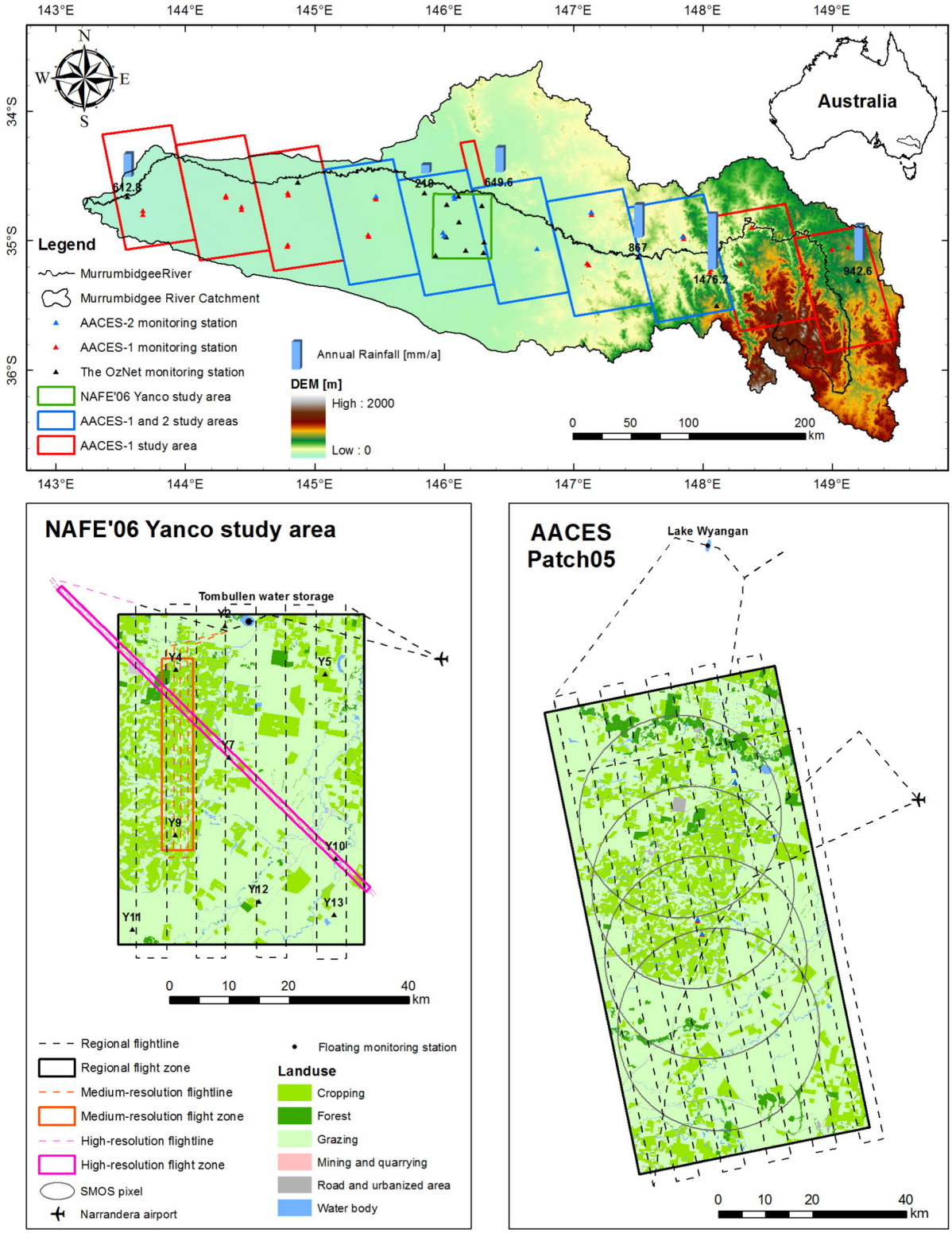

Fig. 1. Location of the NAFE'06 and AACES study areas in the Murrumbidgee River Catchment, southeast of Australia. Location of Tombullen and Wyangan calibration lakes is shown in the lower panels.

surface soil moisture, soil temperature and rainfall measurements across OzNet monitoring stations within the Yanco study area during the period of the NAFE'06, while Fig. 3 shows the same time series during the period of AACES-1. In the AACES, additional monitoring stations were temporally installed in the study areas to collect the temporal variation of rainfall, soil moisture at 0–6 cm (vertically installed) and 25 cm (horizontally installed) depths, soil temperature at depth of 2.5 cm, 5 cm, 15 cm, and 40 cm, soil surface temperature using a thermal infrared sensor, and dew presence using a leaf wetness sensor.

In the calibration lakes, Tombullen water storage for NAFE'06 and Lake Wyangan for AACES, a floating monitoring station was installed in the centre of the lake for continuous measurement of surface water temperature and salinity during the whole period of each campaign. The middle panels of Figs. 2 and 3 illustrate the time series of water

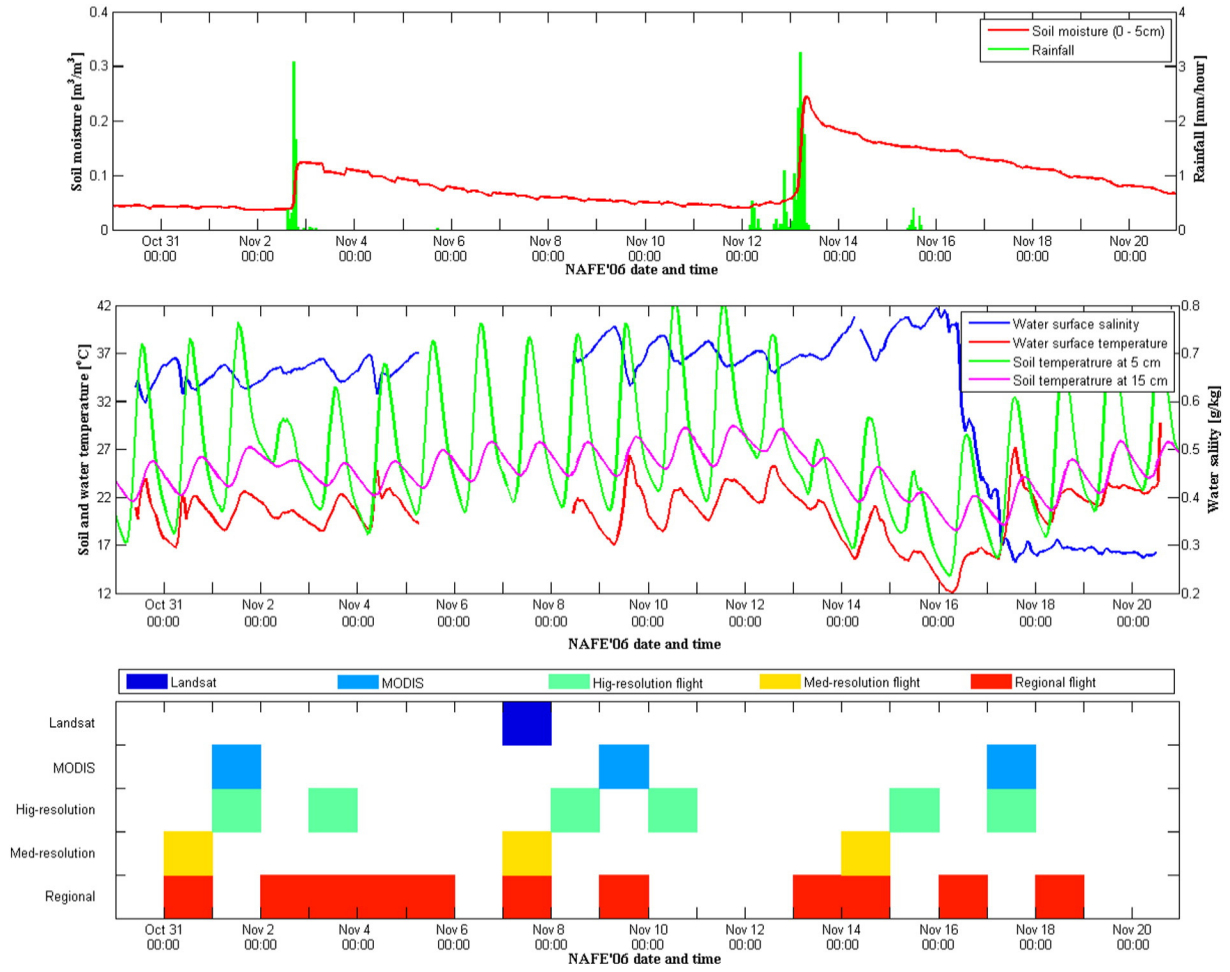

Fig. 2. The NAFE'06 time series of spatially averaged soil moisture and rainfall measurements across all OzNet monitoring stations within the Yanco study area (upper panel), time series of water surface salinity and water surface temperature of Tombullen water storage, together with soil temperature measurements collected from Y2 site (middle panel), and timetable of Landsat overpass, MODIS overpasses and PLMR flights at multiple resolutions (lower panel).

salinity and temperature. Additionally, the spatial variability of surface water temperature and salinity was examined by making point-based measurement transects from a boat. This transect sampling was conducted once a week during the NAFE'06 and the AACES. The transect measurements showed small variations of water surface temperature (±2 K) and salinity (±4 ppm) across the calibration lakes, which would induce a brightness temperature uncertainty of less than 3 K for the water bodies. Given the up to 100 K brightness temperature difference between water and soil, this was ignored for the purpose of this analysis, and the calibration lakes assumed as homogeneous water bodies in this study.

2.3. NAFE'06 campaign

The NAFE'06 was conducted during the Australian summer period from 30th October to 20th November 2006 over two 40 km × 50 km areas, i.e. the Yanco and Kyeamba study areas. The main objective of the NAFE'06 was to collect airborne L-band passive microwave observations at high resolution (50 m to 1000 m) for the development and validation of SMOS soil moisture retrieval, downscaling, and assimilation approaches at SMOS 40 km scale. Since a significant fraction of the land surface over the Yanco study area was irrigated cropping areas, such as rice fields that were consistently flooded during the campaign, data over the Yanco study area is used to investigate the standing water effect in this study. According to the time series of spatially averaged rainfall and soil moisture measurements across the OzNet stations within the Yanco study area (Fig. 2), the land surface varied from very dry conditions at the beginning of the campaign, to drying down after a rainfall of 5.8 mm on 2nd November, and then experiencing a heavy rainfall of total 15 mm on 12th and 13th November. This temporal variation of the Yanco study area was captured by airborne PLMR brightness temperature observations at three spatial resolutions, 50 m (high), 250 m (medium), and 1000 m (regional), respectively. Additionally, multi-angular brightness temperature observations over the high resolution flight zone were also collected on the same day as the high resolution flight.

2.4. AACES campaigns

The AACES series of campaigns were designed to provide airborne L-band brightness temperature observations concurrently with SMOS overpasses under summer (AACES-1) and winter (AACES-2) conditions, in order to calibrate and validate SMOS brightness temperature observations and soil moisture products. The 1-km brightness temperature observations over ten 50 km × 100 km flight patches across the Murrumbidgee River Catchment were collected using the PLMR with the same configuration as in the NAFE'06. Each flight patch contained two independent (or four overlapped) SMOS pixels. The ACCES-1 was conducted over all ten flight patches during 18th January to 21st February 2010. Due to the homogeneity of the first four and last three AACES patches, only Patches 05 to 08 were re-sampled during the AACES-2 being from 8th to 26th September 2010.

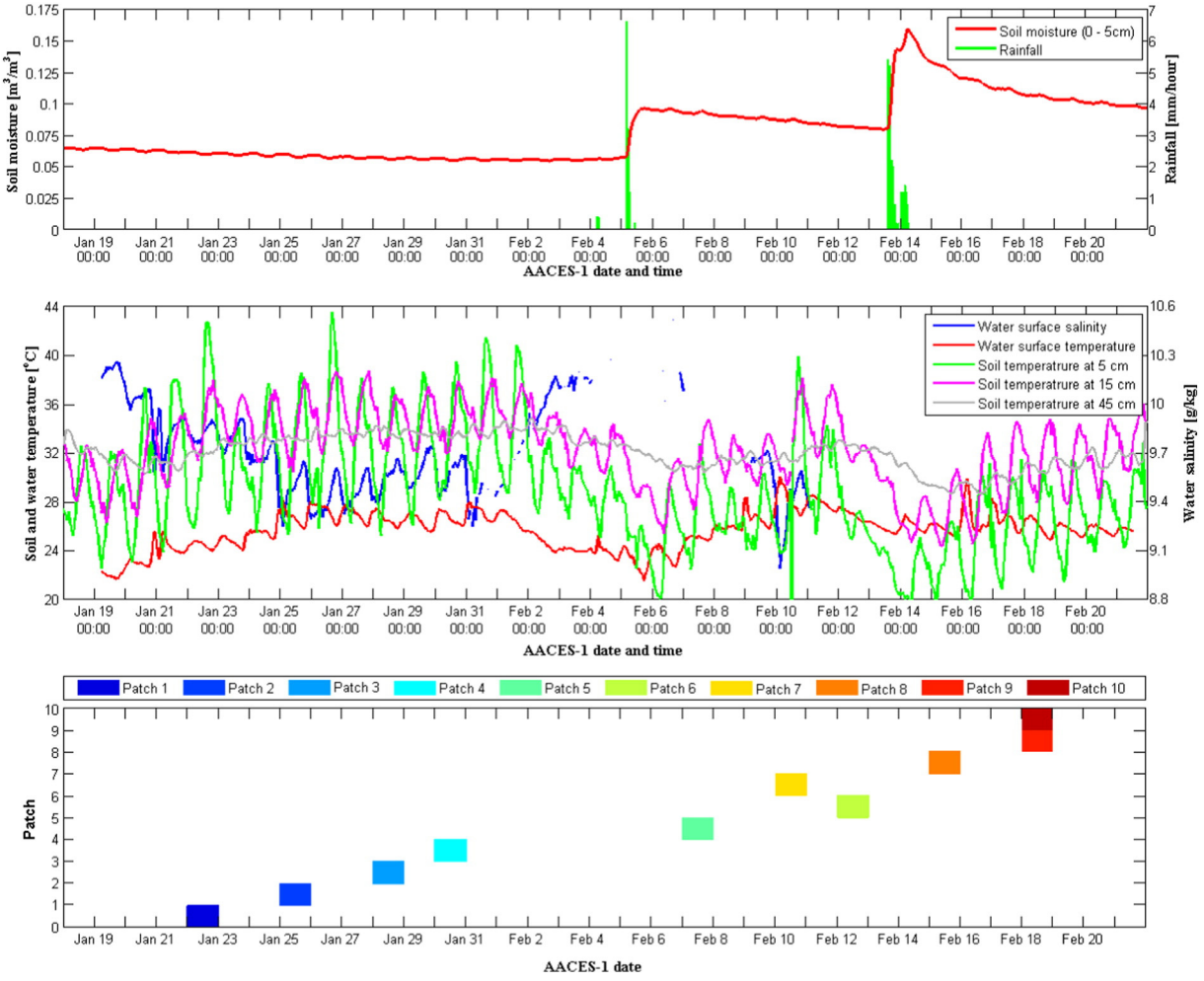

Fig. 3. The AACES-1 time series of soil moisture and rainfall measurements collected from the monitoring stations in Patch 05 site (upper panel), time series of water surface salinity and water surface temperature of Lake Wyangan, together with soil temperature measurements from M7 site (middle panel), and timetable of the AACES-1 flights (lower panel).

2.5. Standing water distribution data

To investigate the effects of water fraction, the information about distribution of open water bodies is required. Currently, a number of methods have been developed to extract inland water extent using remotely sensed visible/infrared (e.g., Landsat, Moderate-Resolution Imaging Spectro-radiometer (MODIS), and Systeme Probatoire d'Observation de la Terre (SPOT)) and SAR (e.g. RADARSAT, JERS-1, and ERS) observations (Brakenridge, Nghiem, Anderson, & Chien, 2005; Mertes, 2002; Papa, Prigent, Durand, & Rossow, 2006; Prigent, Matthews, Aires, & Rossow, 2001; Smith, 1997). Although microwave sensors are able to penetrate clouds and vegetation, the application of SAR (active microwave remote sensing) to discriminating water targets is adversely affected by the wind roughening effect (Alsdorf, Rodríguez, & Lettenmaier, 2007), and space-borne passive microwave sensors suffer from their coarse spatial resolution (Sippel, Hamilton, Melack, & Choudhury, 1994; Smith, 1997). In contrast, mapping open water bodies using visible/infrared observations is more straightforward. In this study, the Modified Normalized Difference Water Index (MNDWI) was used to detect open water bodies due to its improved capability to delineate water bodies from built-up areas, soil, and vegetation targets (Xu, 2006). According to a synthetic analysis on the dynamic of water index thresholds (Ji, Zhang, & Wylie, 2009), MNDWI has more stable thresholds than other water indices. Therefore, water cover information over the Yanco study area was extracted from a 30-m Landsat image acquired on 7th November 2006.

Although the MNDWI data derived from high resolution space-borne visible/infrared observations have high classification accuracy, their applications are limited by their low revisit frequencies (~30 days on average). For the purpose of estimating the effect of the standing water dynamic spatial distribution, an 8-day cloud free water fraction dataset was used (Guerschman et al., 2011). This MODIS water fraction dataset was developed by the Commonwealth Scientific and Industrial Research Organization (CSIRO) in Australia, using surface reflectance from MODIS bands 5 and 7, the Normalized Difference Vegetation Index, the Normalized Difference Water Index and the Multi-resolution index of Valley Bottom Flatness. The water fraction in a ~500-m grid was estimated from the MODIS visible/infrared data using a classification method which was developed by performing a series of simultaneous classifications using higher resolution Landsat TM data, via an image segmentation algorithm (Mueller & Lymburner, 2010). The 500-m water fraction data are available over Australia since the launch of the MODIS in 2000, and the data for ten years (2001 to 2010) were used in this study.

3. Methodology

The effects of water fraction on SMOS and SMAP brightness temperature observations and soil moisture retrieval accuracy were investigated in three steps as follows:

i) assess the accuracy of the MNDWI derived water cover map from a Landsat image along with the MODIS water fraction data, using the high and regional resolution brightness temperature observations collected from the NAFE'06 and AACES;

ii) examine the effect of water fraction on brightness temperature, using the multi-resolution and multi-temporal observations collected from the NAFE'06, as well as the AACES observations collected from multiple land surface conditions;
iii) compare observed effect of water fraction with model simulation; and
iv) identify the SMOS pixels potentially affected by standing water over Australia, using a water fraction threshold for the SMOS/SMAP target accuracy of 0.04 m^3/m^3.

4. Assessment of water cover and fraction maps

The multi-angular brightness temperature observations over water-free areas, and the high resolution brightness temperature observations over Tombullen water storage collected during the entire NAFE'06, were grouped for incidence angles from 0° to 50° in 5° steps and plotted in Fig. 4. It is clear that a brightness temperature difference of ~150 K exists between water bodies and various land surface conditions. While Fig. 2 shows the soil moisture, soil temperature, water salinity and water temperature variation during the NAFE'06, the box and whisker plot in Fig. 4 shows the corresponding brightness temperature impact for the water body and land surface over the Yanco study area during the same period. Consequently, a conservative brightness temperature threshold of 120 K in horizontal polarization and 150 K in vertical polarization was chosen for the reference incidence angle of 38.5°, to distinguish homogeneous water pixels from those for soil surfaces. Consequently, a binary (1 for water fully covered pixel or 0 for the others) water cover map was generated from the NAFE'06 High resolution brightness temperature observations, and used as a reference to assess the accuracy of the water cover maps derived from Landsat data using the MNDWI method.

This threshold method is unsuitable for the brightness temperature observations at the medium and regional resolutions, due to the individual open water bodies in the Yanco study area typically being on order of ~100 m across, meaning that most of the pixels at these scales were either water-free or only partially covered with standing water. Moreover, the limited sampling area covered by the high resolution

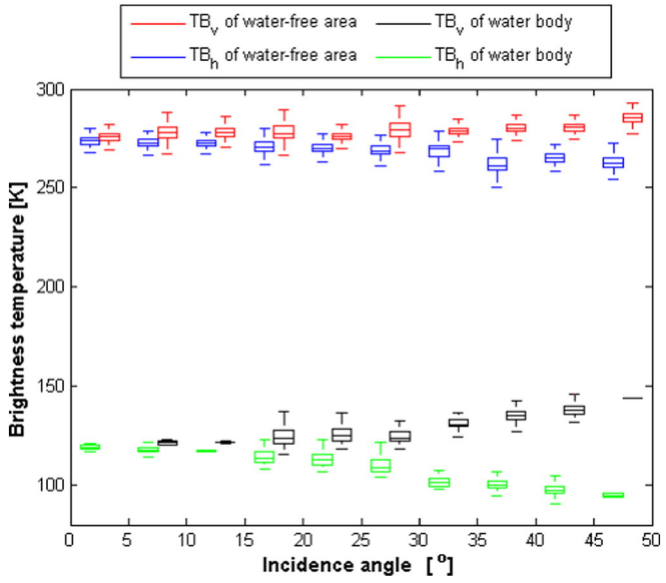

Fig. 4. The angular relationship of dual-polarized brightness temperature observed over water-free areas during the multi-angular flights and over Tombullen water storage during the regional flights within the entire period of the NAFE'06. The brightness temperature observations are grouped in 5° steps. The box and whisker illustrate the distribution of brightness temperature observations in each incidence angle step. The central mark and the edges of the box are the median, the 25th and 75th percentiles. The whiskers show the most extreme data points without consideration of outliers.

(50-m) brightness temperature observations meant that its derived water cover map could not be used to assess the accuracy of the 500-m resolution MODIS water fraction map. Thus, the Landsat-derived water cover map acquired on 7th November 2006 using the MNDWI approach was used for validation of the MODIS water cover fraction product. The regional resolution brightness temperature observations collected during the NAFE'06 and AACES were also used to verifying the accuracy of the MODIS water fraction indirectly, by assessing the correlation between its water fraction and the water induced brightness temperature offset.

According to the bottom panel of Fig. 2, there is only one Landsat overpass during the NAFE'06 campaign, being on 7th November 2006 when no high resolution brightness temperature observations were collected. However, as the upper panel of Fig. 2 shows that there was no rainfall event between 7th and 8th Novermber, and that the open water bodies within the Yanco study area were understood to be temporally static during such short time periods, it was assumed that a water cover map derived from the Landsat image on 7th November 2006 represented the conditions on 8th November 2006.

Fig. 5 shows the brightness temperature and Landsat-derived water cover maps. The grey colour indicates the areas where high resolution brightness temperatures were observed using the PLMR, thus they were compared at pixel level using the two methods. The comparison shows a 98.25% agreement between observed pixels using the brightness temperature threshold and the MNDWI methods. Therefore, the accuracy of the water cover map derived from the Landsat data using the MNDWI method was confirmed and the water cover map on 7th November 2006 used to identify pixels fully covered with standing water.

The 30-m resolution Landsat derived water cover map was integrated to a water fraction map at 500-m resolution, and used as the reference to assess the accuracy of the MODIS water fraction dataset. The Landsat derived water fraction map had a good agreement with the MODIS water fraction dataset at scales from 5 km to 40 km. The regional resolution brightness temperature observations made during the NAFE'06 and AACES campaigns were then sampled to a 1-km grid that overlays the 500-m grid of the MODIS water fraction dataset. The corresponding MODIS water fraction data were also integrated to the same spatial resolution and compared with the corresponding brightness temperature data. Fig. 6 shows an example brightness temperature map at horizontal polarization together with the MODIS water fraction map for 9th November 2006. It is clear that the two maps have a similar pattern between the pixels with standing water coverage and the pixels with lower brightness temperature values.

5. Water fraction effects on brightness temperature

The water fraction effects on brightness temperature, and thus the derived soil moisture retrieval accuracy, were studied using brightness temperature observations collected under multiple scales, sampling dates, and land surface conditions during the NAFE'06 and AACES campaigns.

5.1. Water fraction effects at multiple scales

To decouple the impact of scale from those of other factors, multi-resolution brightness temperature observations were used for the same area and sampling day. However, only the Regional and Medium resolution flights were conducted on 7th November 2006, when the Landsat-derived water cover data were available. However, the distribution of standing water can be assumed similar between 7th and 8th November, due to its make up being primarily small farm dams and flood irrigated rice fields. Additionally, the time series of top 5 cm soil moisture measurements in Fig. 2 show nearly consistent soil moisture measurements between these two days.

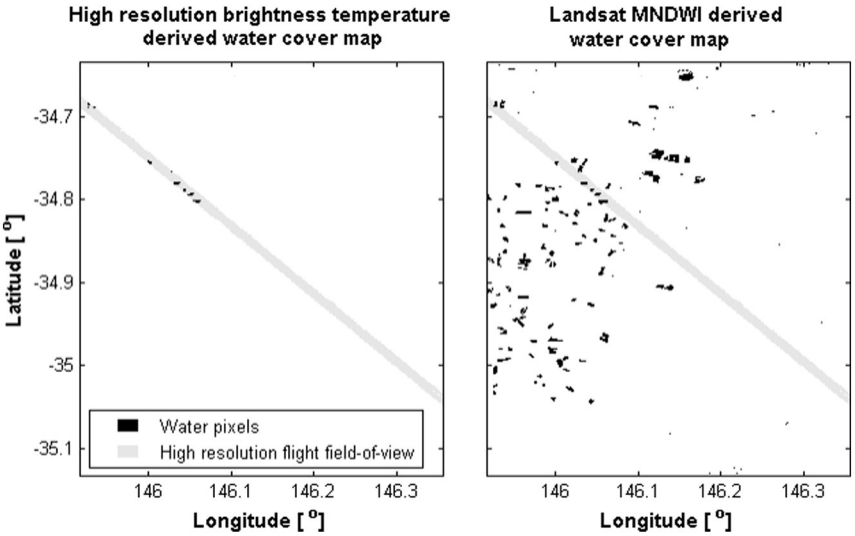

Fig. 5. The water cover maps derived from the airborne high resolution brightness temperatures using the threshold method (left) and the Landsat visible/infrared data using the MNDWI method over the Yanco study area (right).

The middle panel of Fig. 2 also shows a similar diurnal variation of soil temperature at the depth of 5 cm and 15 cm. Although the water temperature and salinity measurements were missing between 7th and 8th November, the adjacent data suggest that it is reasonable to assume the salinity of the calibration lake was stable during this time period, and the variation of surface water temperature similar, since its time series pattern was very close to that of 15-cm depth soil temperature. Hence, the high resolution PLMR observations collected on 8th November 2006 were assumed the same as what would have been observed on 7th November 2006. Subsequently, the multi-resolution brightness temperature observations were sampled to the nested grids, by selecting the brightness temperature nearest to the centre point of the given pixel. The water cover fraction map for each scale was generated by sampling the 30-m Landsat-derived water cover map using the MNDWI method with a threshold of zero (Xu, 2006).

Fig. 7 shows the regional, medium, and high resolution brightness temperature observations at horizontal polarization, and the water cover map derived from the Landsat data for 7th November 2006 over the NAFE'06 medium resolution flight area. A good agreement between the distribution of brightness temperature and that of standing water was found, with the areas identified as water bodies having a very low brightness temperature compared to the surrounding water-free areas. Subsequently, the multi-resolution PLMR brightness temperature observations over the NAFE'06 medium resolution flight area were compared with corresponding water fraction maps at pixel level.

The comparison results are shown in Fig. 8, with whiskers indicating the standard deviation of brightness temperature observations at each water fraction interval. Since the heterogeneity of brightness temperature increases with spatial resolution, the standard deviation of high resolution brightness temperature is significantly larger than those of medium and regional resolution observations.

As anticipated, all four poly-lines representing the three resolutions within the overlapped areas show a decrease of brightness temperature with increasing pixel water fractions. Moreover, the slopes of brightness temperature to water fraction are similar among the regional, medium, and high resolution data with only a small bias between them, which might be due to the change of soil surface temperature between the different resolutions flights. Therefore, the effects of water fraction on

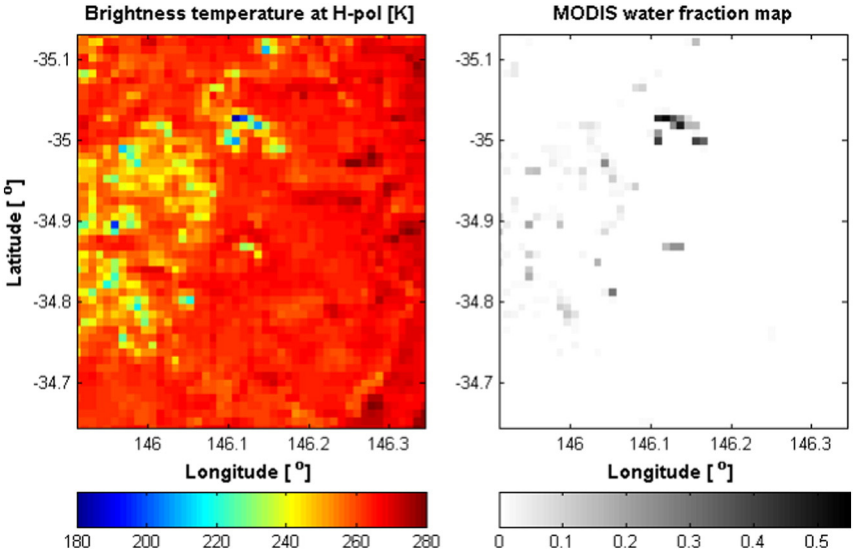

Fig. 6. Maps of airborne brightness temperature observations at horizontal polarization (left) and MODIS-derived water fraction data over the Yanco study area (right) on 9th November 2006.

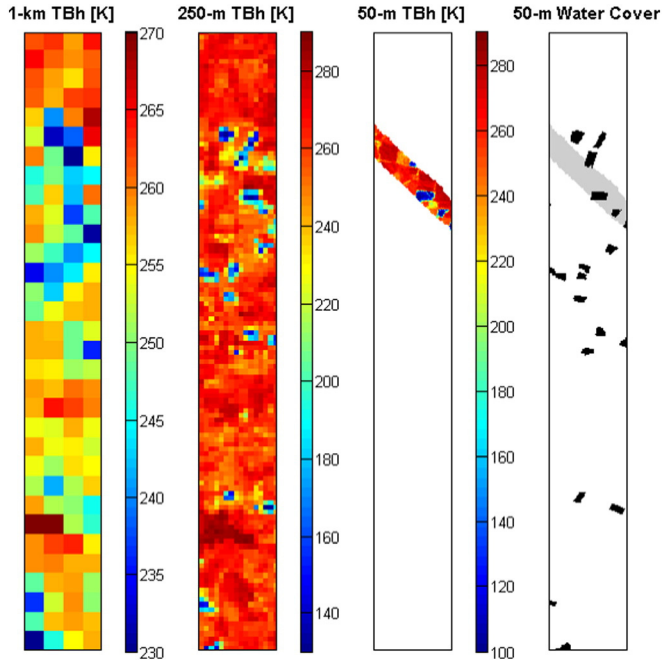

Fig. 7. Horizontally polarized brightness temperature observations at multiple resolutions, together with the Landsat derived water cover data using the MNDWI classification method. Data are plotted for the medium resolution flight zone in the Yanco study area.

brightness temperature, and thus the impact on soil moisture retrieval accuracy were shown to be independent of observation scale. Consequently, the effects of water fraction at the SMOS/SMAP scale can be studied using the regional resolution brightness temperature observations hereafter.

5.2. Water fraction effects at multiple times

During the NAFE'06, a total of 11 regional resolution flights were conducted over the entire Yanco study area, and used here to investigate the temporal variation of water fraction effects. Given the 500-m spatial resolution and 8-day composite of MODIS-derived water fraction data, the water fraction data were integrated to the 1-km regional grid and compared with the regional resolution brightness temperature

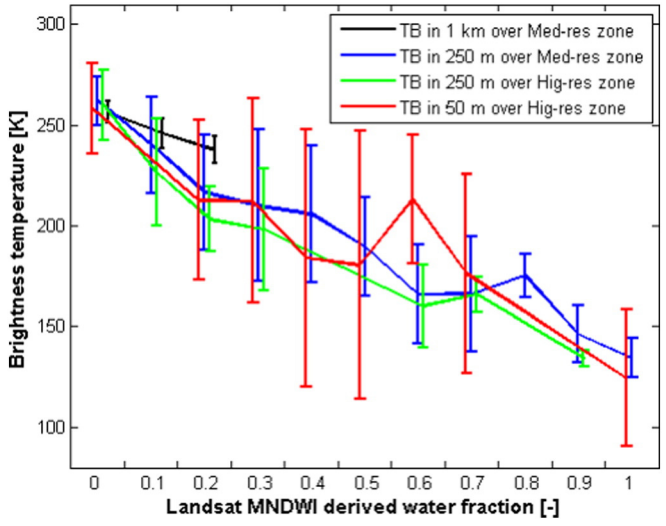

Fig. 8. Relationship between pixel water fraction and mean brightness temperature for the overlapping areas of the high, medium, and regional resolution flights within the medium and high resolution flight zones. The whiskers show the standard deviation of brightness temperature observations for each water fraction step.

observations collected on the same day or one day before/after, as long as no rainfall event had occurred.

To obtain the relationship between water fraction and its effect on brightness temperature at SMOS/SMAP scale, a moving window technique was applied to simulate the SMOS and SMAP 40-km brightness temperature observations with varying water fractions. The regional resolution brightness temperature and MODIS water fraction of all 1-km pixels within a 40 km × 40 km window were averaged to simulate the SMOS/SMAP brightness temperature observations TB_{SMOS} and their water fractions f_{water} respectively. Meanwhile, the mean brightness temperature of water-free pixels TB_{free} was assumed as the reference SMOS/SMAP brightness temperature observations without water fraction effects. Hence, a water induced brightness temperature offset (ΔTB_{water}) on the interpretation of brightness temperature observations can be defined as the difference between TB_{SMOS} and TB_{free}.

By moving the 40 km × 40 km window within the Yanco study area, a limited range of water fraction (<0.003) were obtained, which is insufficient to cover the water fraction threshold for the SMOS/SMAP error budget. For a wider range of water fractions, the size of the moving window was gradually reduced to 5 km, assuming that the water fraction effects obtained from a smaller scale are the same as those at the 40-km scale. The soundness of this assumption has been confirmed already in this paper from the multi-resolution study.

Fig. 9 presents the relationship between water fraction and water induced brightness temperature offset at horizontal and vertical polarizations using the NAFE'06 regional resolution brightness temperature observations and MODIS water fraction data. The symbol colour indicates the mean soil moisture measurements across the OzNet monitoring stations within the Yanco study area. This relationship was also simulated by modelling the brightness temperature of a water body and vegetated soil with ground measured water content, using the L-MEB model (Wigneron et al., 2007). The ancillary data and parameters required by the model were from Merlin et al. (2008).

As expected, both observed and simulated standing water induces a negative brightness temperature offset at both polarizations, whose magnitude varies linearly with increased pixel water fractions. Steeper slopes of the horizontally polarized brightness temperature data indicate higher sensitivity to standing water compared to the vertically polarized brightness temperature. Since these multi-temporal brightness temperature observations were collected over the same area during about three weeks, soil texture and vegetation water content were assumed constant through time, and that the variation of slope was dependent mainly on soil moisture. The dryer the surrounding soil the larger the water induced brightness temperature offset observed, which is in agreement with the simulation results. According to Fig. 9, approximately every 0.1 increase in water fraction results in a brightness temperature offset over 10 K under dry conditions. For a 4-K brightness temperature error budget, being the target for SMOS, a conservative water fraction of 0.04 can be tolerated in soil moisture retrieval providing all other factors are minimal. Due to the uncertainty of water fraction and variation of soil brightness temperature in the moving window, the simulated water effect that assumes a consistent soil component is slightly different from the observed result.

5.3. Water fraction effects at multiple land surface conditions

The effects of water fraction were further investigated under a wider range of soil and vegetation conditions, using the AACES regional resolution brightness temperature observations. The moving window technique was again used to establish the relationship between MODIS-derived water fraction data and water induced brightness temperature offset for each AACES patch. To minimize the effect of land surface heterogeneity, only the patches with a water body larger than 1.25 km^2, thus taking a fraction of 0.05 in a 5 km × 5 km pixel, were considered. The observed and model simulated water fraction effects on brightness temperature at horizontal polarization are plotted in Fig. 10. The soil

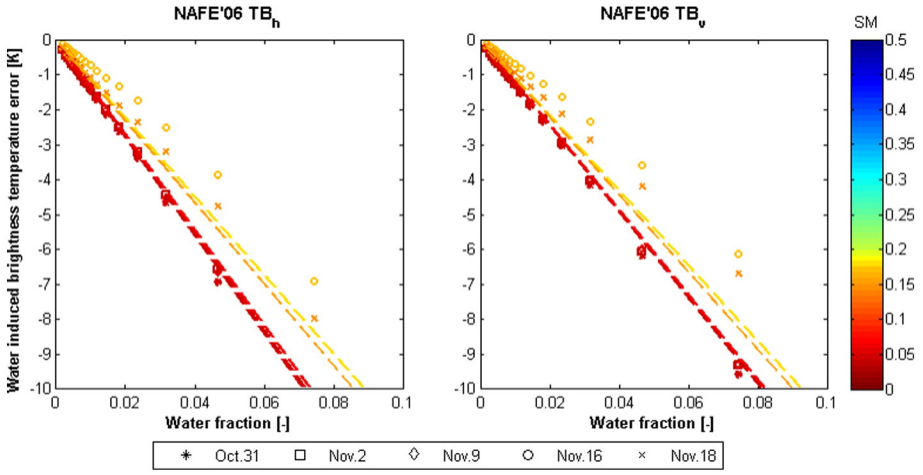

Fig. 9. The relationship between water fraction and water induced brightness temperature impact coloured according to background soil moisture content. The symbols are derived from the NAFE'06 multi-temporal observations while the dashed lines show the model simulated results for the corresponding soil moisture content. Results are shown for both horizontal and vertical polarizations.

moisture in the plot was taken as the mean soil moisture measurement across AACES monitoring stations within each patch.

It is again clear that the ratio between water fraction and induced brightness temperature uncertainty decreases with increase in soil moisture. Compared with the NAFE'06, the effect of water fraction was larger under the AACES-1 hot summer conditions, where every 0.1 increase in water fraction would induce an approximately 20-K brightness temperature offset. During the AACES-2 when vegetation water content was higher and soil temperature was lower than in the AACES-1, the water fraction offset was still mainly dependent on soil moisture. Consequently, every 0.1 increase in water fraction induced a brightness temperature offset ranging from 20 K under hot dry conditions to only 5 K under wet cold conditions. Accordingly, the water fraction threshold for the 4-K error budget varied from 0.02 to 0.08 for dry soil to wet soil conditions respectively.

6. Estimation of water effects on the SMOS and SMAP pixels over Australia

Using the MODIS water fraction data for years 2001 to 2010, the water effects that would have been expected on brightness temperature, and thus derived soil moisture retrieval accuracy, over the entire Australia were estimated at the SMOS/SMAP scale. Due to the similar pixel size of the SMOS 45-km DGG (Discrete Global Grid; Sahr, White, & Kimerling, 2003) and SMAP 36-km EASE (Equal-Area Scalable Earth; Brodzik, Billingsley, Haran, Raup, & Savoie, 2012) grid, only the results on the SMOS grid are presented. For the MODIS-derived water fraction data of each sampling day, the 500-m water fraction grid were resampled to the SMOS grid, assuming that the pixel was a circle centred on a DGG node with a diameter of 45 km. Due to the overlapping nature of the SMOS observations, the water fraction effect is plotted on a Voronoi polygon grid generated from the SMOS DGG points.

The panels (a), (b), and (c) of Fig. 11 show the minimum, maximum, and mean water fraction respectively of each SMOS pixel during the period 2001 to 2010. It is clear that most of Australia had a maximum water fraction less than 0.05, while some areas experienced heavy rain events leading to more than 0.4 of the land surface being flooded. If a static inland water fraction map was used in the soil moisture retrieval model, to correct or flag the effect of standing water, a large uncertainty on brightness temperature and thus retrieved soil moisture could be induced by ignoring the dynamic standing water contribution. Assuming the mean water fraction as the static inland water fraction map, the largest water fraction estimation error likely to be made was approximated by the maximum water fraction shown in Fig. 11(b), as the mean water fraction was generally close to zero.

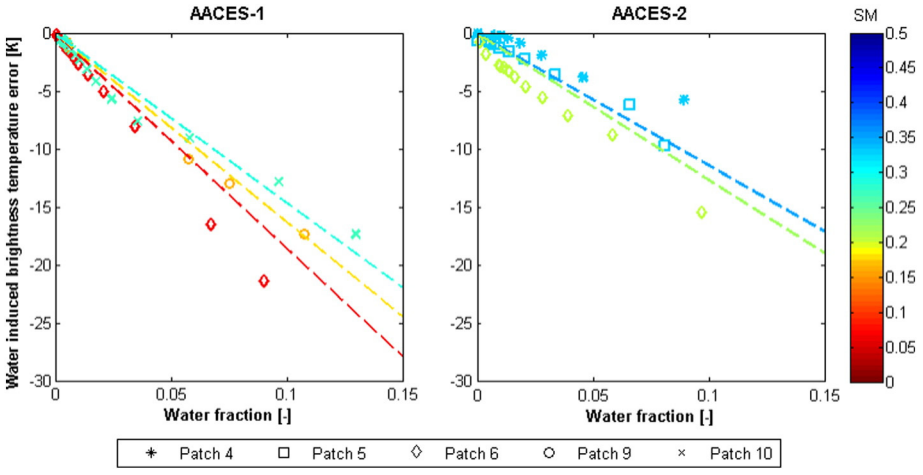

Fig. 10. The relationship between water fraction and water induced brightness temperature impact. The symbols are derived from the AACES multi-spatial observations while the dashed lines show the model simulated results for the corresponding soil moisture content. Results are shown for horizontal polarization only.

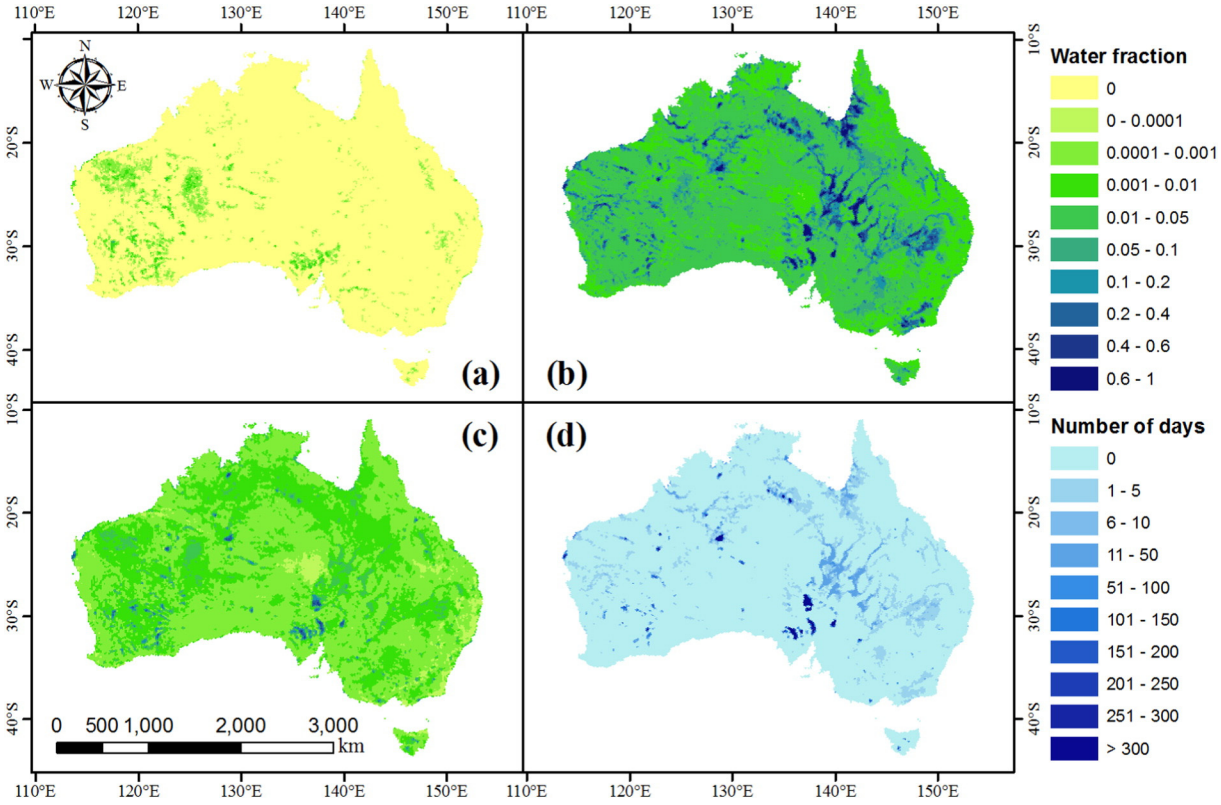

Fig. 11. Maps of minimum (a), maximum (b), and mean (c) water fractions of 40-km sized pixels over Australia during the years from 2001 to 2010. Panel (d) shows the number of days when water fraction of each pixel exceeded the 0.08 water fraction threshold.

Table 1 provides a statistics summary of the minimum, maximum, and mean water fraction of SMOS pixels over Australia during the ten year period 2001 to 2010. In addition, the maximum variation from the mean water fraction was also counted for each water fraction interval, and the corresponding water induced brightness temperature offset estimated. A water fraction of 0.08 was taken as an optimistic threshold for the 4-K brightness temperature "error" budget of SMOS for general soil moisture and vegetation conditions. In the worst case of maximum water fraction there were 13.5% (5,227 out of a total 38,617) land pixels expected to have a soil moisture retrieval error that exceeds the target accuracy of 0.04 m^3/m^3, if the mean water fraction was used as the static water fraction map to apply brightness temperature "corrections". Additionally, the number of days when water fraction exceeded the 0.08 water fraction threshold is shown in Fig. 11(d) for each pixel. According to the summary of water affected pixels in Table 2, although 86.8% of pixels were not affected by the presence of standing water, the standing water induced error would still have exceeded the target accuracy more than 10 times per year on average for 0.6% (252 out of a total 38,617) of Australian land pixels.

7. Conclusion

The effect of water fraction on brightness temperature was studied using multi-scale, multi-temporal, and multi-spatial brightness temperature observations collected from the NAFE'06 and AACES-1 and −2 airborne field experiments. The relationship between water fraction and water induced uncertainty was confirmed to be independent of spatial scale. However, a dependence of this relationship on soil moisture was found. The tolerable thresholds of water fraction for achieving a maximum 4-K brightness temperature offset obtained from field experiment data were found to range from 0.02 to 0.08 under the conditions from dry bare soil to wet vegetated soil.

The dynamic of water fraction effects were also investigated using MODIS-derived water fraction data for a ten year period from 2001 to

Table 1
Statistics of water fraction and induced brightness temperature offset of SMOS sized pixels over Australia according to Fig. 11.

Water fraction range	Estimated water induced brightness temperature impact	Percentage of land pixels in range for the minimum water fraction mask	Percentage of land pixels in range for the maximum water fraction mask	Percentage of land pixels in range for the mean water fraction mask	Percentage of land pixels with a water fraction variation in the range
[−]	[K]	[%]	[%]	[%]	[%]
0	0	89.5	0.0	0.0	0
0–0.0001	0–0.005	5.9	0.0	3.0	0
0.0001–0.001	0.005–0.05	3.6	0.0	55.5	0.04
0.001–0.01	0.05–0.5	0.9	20.4	34.7	22.4
0.01–0.05	0.5–2.5	0.0	57.7	5.2	57.3
0.05–0.1	2.5–5	0.0	9.8	0.7	9.1
0.1–0.2	5–10	0.0	6.3	0.5	5.9
0.2–0.4	10–20	0.0	3.7	0.3	3.5
0.4–0.6	20–30	0.0	1.3	0.1	1.1
0.6–1	30–50	0.0	0.9	0.0	0.6

Table 2
Statistics of water effected land pixels at SMOS scale over Australia for 2001 to 2010.

Number of days	Number of pixels	Percentage of pixels [%]
0	33,514	86.8
1–5	3,426	8.9
6–10	550	1.4
11–50	779	2.0
51–100	96	0.3
101–150	29	0.1
151–200	46	0.1
201–250	21	0.1
251–300	33	0.1
>300	123	0.3

2010. The map of mean water fraction for SMOS pixels across the ten years was used as a static water cover map for flagging or correcting standing water effects. Taking 0.08 as the highest threshold of water fraction for achieving the SMOS and SMAP 0.04 m^3/m^3 target accuracy of soil moisture without water correction, there were 13.5% land pixels over Australia that would have been significantly affected by water bodies in the assumed worst case that all pixels reached their maximum water fraction simultaneously. In reality, 86.8% of pixels would not have been affected by the presence of standing water, while 0.6% of land pixels would have had a water induced brightness temperature offset that would have exceeded the allowable threshold more than 100 times during the 2001 and 2010 period.

Acknowledgements

This study has been conducted within the framework of the MoistureMap project funded by the Australian Research Council (DP0879212). The airborne and ancillary ground data used in this work were also collected with the support of earlier funding from the ARC for infrastructure (LE0453434) and research (DP0209724 and DP0557543), the National Aeronautics and Space Administration, and the goodwill of many volunteers during the NAFE'06 and AACES field campaigns.

References

Alsdorf, D.E., Rodríguez, E., & Lettenmaier, D.P. (2007). Measuring surface water from space. *Reviews of Geophysics, 45*.
Aubert, D., Loumagne, C., & Oudin, L. (2003). Sequential assimilation of soil moisture and streamflow data in a conceptual rainfall–runoff model. *Journal of Hydrology, 280*, 145–161.
Australian Bureau of Rural Science (2001). *Mean monthly and mean annual rainfall and temperature data*. Melbourne, Australia: Bureau of Meteorology, Australia.
Brakenridge, G.R., Nghiem, S.V., Anderson, E., & Chien, S. (2005). Space-based measurement of river runoff. *Transactions on American Geophysical Union, 86*, 185–188.
Brodzik, M.J., Billingsley, B., Haran, T., Raup, B., & Savoie, M.H. (2012). EASE-Grid 2.0: Incremental but significant improvements for earth-gridded data sets. *ISPRS International Journal of Geo-Information, 1*, 32–45.
Choudhury, B., Schmugge, T., & Mo, T. (1982). A parameterization of effective soil temperature for microwave emission. *Journal of Geophysical Research, 87*, 1301–1304.
Crow, W.T., Berg, A.A., Cosh, M.H., Loew, A., Mohanty, B.P., Panciera, R., de Rosnay, P., Ryu, D., & Walker, J.P. (2012). Upscaling sparse ground-based soil moisture observations for the validation of coarse-resolution satellite soil moisture products. *Reviews of Geophysics, 50*, RG2002.
Davenport, I.J., Sandells, M.J., & Gurney, R.J. (2008). The effects of scene heterogeneity on soil moisture retrieval from passive microwave data. *Advances in Water Resources, 31*, 1494–1502.
Entekhabi, D., Njoku, E.G., O'Neill, P.E., Kellogg, K.H., Crow, W.T., Edelstein, W.N., Entin, J.K., Goodman, S.D., Jackson, T.J., & Johnson, J. (2010). The soil moisture active passive (SMAP) mission. *Proceedings of the IEEE, 98*, 704–716.
Gouweleeuw, B.T., van Dijk, A.I.J.M., Guerschman, J.P., Dyce, P., & Owe, M. (2012). Space-based passive microwave soil moisture retrievals and the correction for a dynamic open water fraction. *Hydrology and Earth System Sciences, 16*, 1635–1645.
Guerschman, J.P., Warren, G., Byrne, G., Lymburner, L., Mueller, N., & Van Dijk, A.I.J.M. (2011). *MODIS-based standing water detection for flood and large reservoir mapping: Algorithm development and applications for the Australian continent: CSIRO.*
Jackson, T.J. (2001). Multiple resolution analysis of L-band brightness temperature for soil moisture. *IEEE Transactions on Geoscience and Remote Sensing, 39*, 151–164.
Ji, L., Zhang, L., & Wylie, B. (2009). Analysis of dynamic thresholds for the normalized difference water index. *Photogrammetric Engineering and Remote Sensing, 75*, 1307–1317.
Kerr, Y.H., Waldteufel, P., Richaume, P., Davenport, I., Ferrazzoli, P., & Wigneron, J. -P. (2010a). *SMOS level 2 processor soil moisture algorithm theoretical basis document (ATBD)*. SM-ESL (CBSA), CESBIO, Toulouse, SO-TN-ARR-L2PP-0037, Issue 3.4.
Kerr, Y.H., Waldteufel, P., Wigneron, J. -P., Delwart, S., Cabot, F., Boutin, J., Escorihuela, M.J., Font, J., Reul, N., & Gruhier, C. (2010b). The SMOS mission: New tool for monitoring key elements of the global water cycle. *Proceedings of the IEEE, 98*, 666–687.
Kim, S., van Zyl, J., Dunbar, S., Njoku, E.G., Johnson, J., Moghaddam, M., Shi, J., & Tsang, L. (2012). *SMAP L2 & L3 Radar Soil Moisture (Active) Data Products.*
Loew, A. (2008). Impact of surface heterogeneity on surface soil moisture retrievals from passive microwave data at the regional scale: The Upper Danube case. *Remote Sensing of Environment, 112*, 231–248.
Merlin, O., Walker, J.P., Kalma, J.D., Kim, E.J., Hacker, J., Panciera, R., Young, R., Summerell, G., Hornbuckle, J., & Hafeez, M. (2008). The NAFE'06 data set: Towards soil moisture retrieval at intermediate resolution. *Advances in Water Resources, 31*, 1444–1455.
Mertes, L.A.K. (2002). Remote sensing of riverine landscapes. *Freshwater Biology, 47*, 799–816.
Mueller, N., & Lymburner, L. (2010). Extracting landscape features in emergency response situations: Combining fuzzy logic and Gaussian statistics in object-oriented analysis. *15th Australasian Remote Sensing & Photogrammetry Conference (ARSPC)*. Alice Springs.
Olioso, A., Chauki, H., Courault, D., & Wigneron, J.P. (1999). Estimation of evapotranspiration and photosynthesis by assimilation of remote sensing data into SVAT models. *Remote Sensing of Environment, 68*, 341–356.
Panciera, R., Walker, J.P., Kalma, J.D., Kim, E.J., Hacker, J.M., Merlin, O., Berger, M., & Skou, N. (2008). The NAFE'05/CoSMOS data set: Toward SMOS soil moisture retrieval, downscaling, and assimilation. *IEEE Transactions on Geoscience and Remote Sensing, 46*, 736–745.
Papa, F., Prigent, C., Durand, F., & Rossow, W.B. (2006). Wetland dynamics using a suite of satellite observations: A case study of application and evaluation for the Indian subcontinent. *Geophysical Research Letters, 33*.
Peischl, S., Walker, J.P., Rüdiger, C., Ye, N., Kerr, Y.H., Kim, E., Bandara, R., & Allahmoradi, M. (2012). The AACES field experiments: SMOS calibration and validation across the Murrumbidgee River catchment. *Hydrology and Earth System Sciences, 9*, 2763–2795.
Prigent, C., Matthews, E., Aires, F., & Rossow, W.B. (2001). Remote sensing of global wetland dynamics with multiple satellite data sets. *Geophysical Research Letters, 28*, 4631–4634.
Ryu, D., & Famiglietti, J.S. (2006). Multi-scale spatial correlation and scaling behavior of surface soil moisture. *Geophysical Research Letters, 33*, L08404.
Sahr, K., White, D., & Kimerling, A.J. (2003). Geodesic discrete global grid systems. *Cartography and Geographic Information Science, 30*, 121–134.
Schnürer, J., Clarholm, M., Boström, S., & Rosswall, T. (1986). Effects of moisture on soil microorganisms and nematodes: A field experiment. *Microbial Ecology, 12*, 217–230.
Sellers, P.J., Dickinson, R.E., Randall, D.A., Betts, A.K., Hall, F.G., Berry, J.A., Collatz, G.J., Denning, A.S., Mooney, H.A., & Nobre, C.A. (1997). Modeling the exchanges of energy, water, and carbon between continents and the atmosphere. *Science, 275*, 502–509.
Sippel, S.J., Hamilton, S.K., Melack, J.M., & Choudhury, B.J. (1994). Determination of inundation area in the Amazon River floodplain using the SMMR 37 GHz polarization difference. *Remote Sensing of Environment, 48*, 70–76.
Smith, L.C. (1997). Satellite remote sensing of river inundation area, stage, and discharge: A review. *Hydrological Processes, 11*, 1427–1439.
Smith, A.B., Walker, J.P., Western, A.W., Young, R.I., Ellett, K.M., Pipunic, R.C., Grayson, R.B., Siriwardena, L., Chiew, F.H.S., & Richter, H. (2012). The Murrumbidgee soil moisture monitoring network data set. *Water Resources Research, 48*, W07701.
Wigneron, J. -P., Kerr, Y., Waldteufel, P., Saleh, K., Escorihuela, M. -J., Richaume, P., Ferrazzoli, P., De Rosnay, P., Gurney, R., & Calvet, J. -C. (2007). L-band Microwave Emission of the Biosphere (L-MEB) Model: Description and calibration against experimental data sets over crop fields. *Remote Sensing of Environment, 107*, 639–655.
Xu, H. (2006). Modification of normalised difference water index (NDWI) to enhance open water features in remotely sensed imagery. *International Journal of Remote Sensing, 27*, 3025–3033.
Ye, N., Walker, J. P., & Rudiger, C. (2015). A cumulative distribution function method for normalizing variable-Angle microwave observations. *IEEE Transactions on Geoscience and Remote Sensing, 53*, 3906–3916.